Advances in Geo-Energy Research

Vol. 20, No. 3, p. 259-276, 2026

Original article

# Maturity-controlled competitive adsorption of $CO_2$-$H_2$ and $CH_4$-$H_2$ gas mixtures in shale kerogen nanopores

Zhikai Liang[1,2], Zhenxue Jiang[3]*, Mehdi Ostadhassan[4], Guangyou Zhu[1,2], Zhuo Li[3], Muhammad Arif[5]*

[1]*Key Laboratory of Exploration Technologies for Oil and Gas Resources, Ministry of Education, Yangtze University, Wuhan 430100, P. R. China*

[2]*School of Geosciences, Yangtze University, Wuhan 430100, P. R. China*

[3]*State Key Laboratory of Petroleum Resources and Engineering, China University of Petroleum, Beijing 102249, P. R. China*

[4]*Institute of Geosciences, Marine and Land Geomechanics and Geotectonics, Christian-Albrechts-Universitat, Kiel 24118, Germany*

[5]*Department of Chemical & Petroleum Engineering, Khalifa University, Abu Dhabi 127788, United Arab Emirates*

**Keywords:**
Longmaxi shale
molecular structure reconstruction
underground hydrogen storage
competitive adsorption
kerogen
molecular simulation

**Cited as:**
Liang, Z., Jiang, Z., Ostadhassan, M., Zhu, G., Li, Z., Arif, M. Maturity-controlled competitive adsorption of $CO_2$-$H_2$ and $CH_4$-$H_2$ gas mixtures in shale kerogen nanopores. Advances in Geo-Energy Research, 2026, 20(3): 259-276.
https://doi.org/10.46690/ager.2026.06.07

**Abstract:**
Organic-rich shales present significant potential for underground hydrogen storage, yet our understanding of the interactions of $H_2$ with $CH_4$ and $CO_2$ in kerogen-hosted nanopores remain insufficient. This study constructs and validates macromolecular models of high-maturity and overmature kerogens via combining solid-state carbon-13 nuclear magnetic resonance spectroscopy, Fourier-transform infrared spectroscopy, and X-ray photoelectron spectroscopy. Grand canonical Monte Carlo and molecular dynamics simulations are performed, which reveal that kerogen maturity controls the competitive adsorption and diffusion of methane/hydrogen and carbon dioxide/hydrogen mixtures by regulating nanopore structure and surface chemical heterogeneity. Compared with high-maturity kerogen, overmature kerogen shows stronger confinement and a more pronounced near-surface enrichment of $CH_4$ and especially $CO_2$, which reduces the effective storage space available for $H_2$. Mechanistically, $CH_4$/$H_2$ competition is driven by van der Waals interactions, whereas $CO_2$/$H_2$ competition is dominated by stronger electrostatic and inductive interactions, establishing a thermodynamic affinity order. The radial distribution functions and interaction energies are measured, which confirm that $CH_4$ and $CO_2$ monopolize high-energy surface sites, relegating $H_2$ to a weakly adsorbed, bulk-like state. Although $H_2$ exhibits the weakest adsorption affinity, its high mobility suggests a stronger migration tendency and potential leakage risk, which should be considered when evaluating long-term containment security during underground hydrogen storage. Overall, this study reveals that maturity-controlled coupling exists between kerogen structure, competitive adsorption and gas transport, providing molecular-scale insights into hydrogen storage security, injectivity, leakage risk, and recovery in organic-rich shale reservoirs.

## 1. Introduction

Driven by the rapid population growth and accelerating industrial development worldwide, global energy demand has continued to rise sharply (Zou et al., 2019; Jiang et al., 2020). At present, fossil fuels still dominate the global energy supply, contributing nearly 80% of total energy consumption (Mohr et al., 2015). However, their utilization, including that of oil, coal and natural gas, generates substantial greenhouse gas

Yandy Scientific Press

*Corresponding author.
*E-mail address*: liangzhikai2020@163.com (Z. Liang); jiangzx@cup.edu.cn (Z. Jiang); mehdi.ostadhassan@ifg.uni-kiel.de (M. Ostadhassane); zhuguangyou@yangtzeu.edu.cn (G. Zhu); zhuo.li@cup.edu.cn (Z. Li); muhammad.arif@ku.ac.ae (M. Arif).
2207-9963 © The Author(s) 2026.
Received April 10, 2026; revised May 15, 2026; accepted June 3, 2026; available online June 6, 2026.

emissions, thereby exacerbating climate change and global warming (Gustavsson et al., 2017). As a promising clean energy carrier, hydrogen is widely regarded as an important component of the low-carbon energy transition, with significant implications for both economic development and climate change mitigation (Suzuki et al., 2017; Yu et al., 2021). However, the low density and high diffusivity of hydrogen pose major challenges for its large-scale storage in practical energy systems (Tarkowski and Uliasz-Misiak, 2022). In recent years, numerous studies on underground hydrogen storage (UHS) have been conducted, which demonstrated significant progress in evaluating the technical and economic feasibility of different geological structures for UHS (Navaid et al., 2023; Ren et al., 2025). Specifically, deep water-bearing formations, saline formations, salt caverns, underground coal beds, and depleted oil and gas fields are all potential targets for large-scale UHS (Navaid et al., 2023). Among these, exhausted oil and gas reservoirs are beneficial as they possess existing drilling infrastructure and are characterized by familiar in-situ geological conditions (sealing layers, storage capacity, temperature and pressure, rock physical properties, etc.), rendering them a promising candidate for UHS and a focus of extensive research (Sekar et al., 2023).

Shale has recently attracted increasing scientific interest as a potential medium for hydrogen storage and subsequent recovery, particularly in depleted shale gas reservoirs (Wang et al., 2024). Organic-rich shale intervals, characterized by elevated total organic carbon (TOC), are also key targets for unconventional shale gas exploration and development (Bian et al., 2025). Compared to conventional reservoirs, they exhibit a more complex mineral composition, variable TOC content, and extremely low permeability and porosity. However, the high surface area of organic matter (OM) within shale provides abundant adsorption sites for hydrogen, facilitating the adsorption process (including absorption and adsorption), which yields shale gas reservoirs with strong storage capacity (Liu et al., 2024a; Bian et al., 2025). During shale gas production, large-scale horizontal well sections are required for hydraulic fracturing to form artificial fracture networks with high permeability. Once shale gas production declines, directly leveraging existing shale gas production equipment and technology for hydrogen storage can significantly reduce costs. The maturity of OM is one of the key factors influencing shale storage capacity, mechanical properties, and gas content characteristics (Bian et al., 2025). The hydrogen storage process in depleted shale gas reservoirs is inevitably influenced by the OM properties. While the adsorption of $CH_4$ and $CO_2$ in shales has been widely investigated over the past two decades, only a few studies have explored the potential for $H_2$ adsorption in shales. Molecular simulations in several studies have confirmed that $H_2$ adsorption on illite, kaolinite, calcite, dolomite, and quartz surfaces is a predominantly physical process, with only one monolayer of $H_2$ molecules adsorbed (Zhang et al., 2024b). The $H_2$ uptake capacity decreases in the following sequence: kaolinite > illite > calcite > dolomite > quartz, indicating that clay minerals can retain approximately two to three times more $H_2$ than other common mineral phases (Zhao2025). What is more, research on hydrogen adsorption within the kerogen in shale is even more limited (Psarras et al., 2017; Li et al., 2024; Zhang et al., 2024a), which severely restricts our understanding of $CO_2/H_2$ and $CH_4/H_2$ adsorption and storage potential in kerogens of different maturity.

Recent investigations have advanced our understanding of $H_2$ adsorption behavior and migration characteristics within shale nanopores (Zhang et al., 2023; Li et al., 2024). Shale typically presents a Type IV $H_2$ adsorption isotherm, suggesting that nanopore adsorption is mainly governed by physical adsorption. Compared with $CH_4$, $H_2$ exhibits a substantially greater diffusion coefficient, and its diffusivity generally increases at higher temperatures but decreases under elevated pressure (Wang et al., 2024). Multicomponent adsorption analyses involving $H_2$, $CH_4$, $C_2H_6$, $C_3H_8$, and $CO_2$ demonstrated strong gas selectivity, where heavier hydrocarbons exhibited higher adsorption affinity and smaller pores impose stronger confinement effects (Raza et al., 2024). In addition, kinetic and thermodynamic analyses suggested that $H_2$ adsorption in shale and coal is mainly governed by physical interactions and can be described by BET and pseudo-second-order kinetic models (Yang et al., 2025; Xiong et al., 2026). However, most existing studies focus on single-component adsorption or general gas selectivity, while the competitive adsorption and coupled diffusion processes of $H_2$ with residual $CH_4$ or cushion gases such as $CO_2$ remain insufficiently understood. Moreover, the systematic influence of kerogen maturity on $CH_4/H_2$ and $CO_2/H_2$ competitive adsorption mechanisms has not been fully clarified at the molecular scale.

To address the above need, OM samples from the Longmaxi shale were characterized using multiple spectroscopic techniques, including Fourier transform infrared (FTIR) spectroscopy, solid-state carbon-13 nuclear magnetic resonance ($^{13}$C NMR) spectroscopy, laser Raman spectroscopy, and X-ray photoelectron spectroscopy (XPS). Subsequently, on the basis of the experimental findings, kerogen molecular models were constructed representing high-maturity and over-mature stages. These models were equilibrated through successive canonical ensemble and isothermal-isobaric ensemble molecular dynamics simulations to obtain realistic kerogen densities. To clarify how OM maturity affects shale-based UHS, the competitive adsorption characteristics of $CO_2/H_2$ and $CH_4/H_2$ mixtures at different compositions were systematically evaluated, with particular emphasis on adsorption capacity, adsorption heat, diffusion coefficients, and intermolecular interaction energies. By elucidating the coupled transport-adsorption mechanisms of hydrogen within shale OM, this study explores the multicomponent competitive adsorption of hydrogen and its associated mobility and retention. The results are expected to provide critical molecular-scale insights for evaluating the safety of UHS systems and for optimizing injection-production strategies.

## 2. Experiment and analysis

### 2.1 Samples and kerogen isolation

Shale samples were obtained from Longmaxi Formation deposits in the Luzhou area, southern Sichuan Basin, China. This region is located within comparable structural units and

represents an important shale gas production area in China, characterized by favorable reservoir conditions, elevated TOC content, and OM maturity exceeding 3.0% (Wu et al., 2023). In the context of UHS, the Longmaxi shale with high connected porosity and wide distribution allow the stimulated reservoir volume created by hydraulic fracturing to serve as storage space. Furthermore, the surrounding shale acts as a caprock to tightly seal the stimulated reservoir volume and ensure containment (Chen et al., 2026).

In order to separate kerogen from the bulk shale, chemical methods are typically used to dissolve minerals while minimizing changes to the chemical structure of kerogen. Kerogen was isolated by acid digestion, pyrite removal, $ZnCl_2$ heavy-liquid separation, and chloroform extraction according to a previously described protocol (Liang et al., 2024). Carbonates were first dissolved with HCl, whereas quartz, clay minerals, and feldspar were removed using HCl-HF treatment. Pyrite was eliminated by reacting 6 mol/L HCl with arsenic-free zinc granules. The residue was then separated with $ZnCl_2$ heavy liquid, repeatedly rinsed with distilled water, and ultrasonically cleaned in chloroform. Finally, the kerogen was dried, weighed and ground. It is noteworthy that the kerogen extraction process may, to some extent, alter the original pore structure characteristics; therefore, this study characterizes the results based on a representative average kerogen structure.

## 2.2 Spectroscopic investigations

Kerogen chemistry and structural ordering were characterized using XPS, FTIR, XRD, solid-state $^{13}$C-NMR, and Raman spectroscopy. XPS was performed on a Thermo Fisher Nexsa system equipped with a monochromatic aluminum K$\alpha$ source operated at 150 W (Liu et al., 2021). Survey spectra were used to determine the elemental compositions and atomic percentages, whereas high-resolution spectra were collected to identify the chemical states and relative abundances of major elements. Fourier-transform infrared spectra were obtained using a Thermo Fisher Nicolet IS5 spectrometer. Kerogen powder was mixed with potassium bromide at a mass ratio of 1 : 100 and pressed into translucent pellets under 10 MPa; spectra were recorded from 400 to 4,000 $cm^{-1}$ with 32 scans and a resolution of 4 $cm^{-1}$. X-ray diffraction was conducted on a Bruker D8 ADVANCE diffractometer to determine aromatic layer extension, interlayer spacing, and stacking height based on the 002 and 100 reflections. Solid-state carbon-13 nuclear magnetic resonance spectra were acquired using a Bruker Avance III HD spectrometer to quantify aliphatic, aromatic and carbonyl carbon fractions. Raman spectra were collected using a LabRAM HR Evolution spectrometer with a 532 nm laser and 4 $cm^{-1}$ spectral resolution.

## 2.3 Pore structure analysis

The structural characteristics of kerogen nanopores were analyzed via low-pressure $N_2$ and $CO_2$ adsorption using a Micromeritics ASAP 2020 analyzer. Samples (approx. 3 g, 60-120 mesh) were vacuum-dried for 8 h prior to testing. $N_2$ adsorption was conducted at −195.8 °C (101.3 kPa), while $CO_2$ isotherms were obtained at 0 °C for micropore characterization. Pore size distributions were derived from the adsorption data using the density functional theory model.

## 2.4 Molecular structure and adsorption modeling

### 2.4.1 Two-dimensional (2D) molecular structure of kerogen

Previous studies have developed kerogen models for the Longmaxi Formation shale based on core and outcrop samples. To compare structural variations from high to over-mature stages, this study establishes 2D kerogen models for two maturity levels, GU5 and L10, using constrained elemental analysis, XPS, FTIR, and solid-state $^{13}$C NMR results (Hou et al., 2023; Liang et al., 2024). The initial chemical formula was determined based on elemental analysis (Liu et al., 2021). The carbon skeleton, oxygen-containing groups, and N-/S-containing species were then assigned based on $^{13}$C NMR, XPS, and FTIR constraints. Initial 2D kerogen models were constructed by linking these structural fragments and iteratively optimized by comparing MestReNova-predicted $^{13}$C NMR spectra with experimental spectra until satisfactory agreement was achieved (Liu et al., 2021; Hou et al., 2023). Experimental XPS, FTIR and solid-state $^{13}$C NMR data were used to constrain the molecular structures of kerogen, and the reconstructed models were refined and validated by comparing simulated and experimental spectral features (Fig. 1). Details of the reconstruction and validation procedures are provided in the Supplementary material.

### 2.4.2 Establishment of kerogen slit nanopore and simulation details

Guided by the experimental constraints, the elemental composition, aromatic/aliphatic carbon distribution, oxygen-containing functional groups, and N-/S-containing species were assigned to construct representative kerogen molecular fragments. Subsequently, multiple fragments were assembled into periodic cells to build kerogen matrix models, whereas slit nanopores were generated by stacking two kerogen matrix layers (Fig. 2). All simulations were performed using the COMPASS force field, which includes bonded interactions and non-bonded van der Waals forces (Sun et al., 1998). All simulations were conducted using the COMPASS force field, which has been widely applied to organic macromolecules, kerogen-like structures, hydrocarbon systems, and shale nanopore adsorption (Sun et al., 1998; Pan et al., 2022). Previous studies have shown that the COMPASS force field can be applied to the simulation of kerogen-related adsorption processes (Table S1). The Lennard-Jones parameters and partial atomic charges were taken from previous studies (Waldman and Hagler, 2004). The initial kerogen matrix model was generated in the Amorphous Cell module from 10 kerogen with an initial density of 0.01 $g/cm^3$. Geometry optimization was first carried out at 900 K for 100 ps in the NVT ensemble, followed by several NPT runs. The temperature was then gradually decreased from 900 to 330 K to densify the structure (He et al., 2020), yielding final densities of 1.231 $g/cm^3$ and 1.248 $g/cm^3$ for GU5 and L10, respectively, close to experimental kerogen

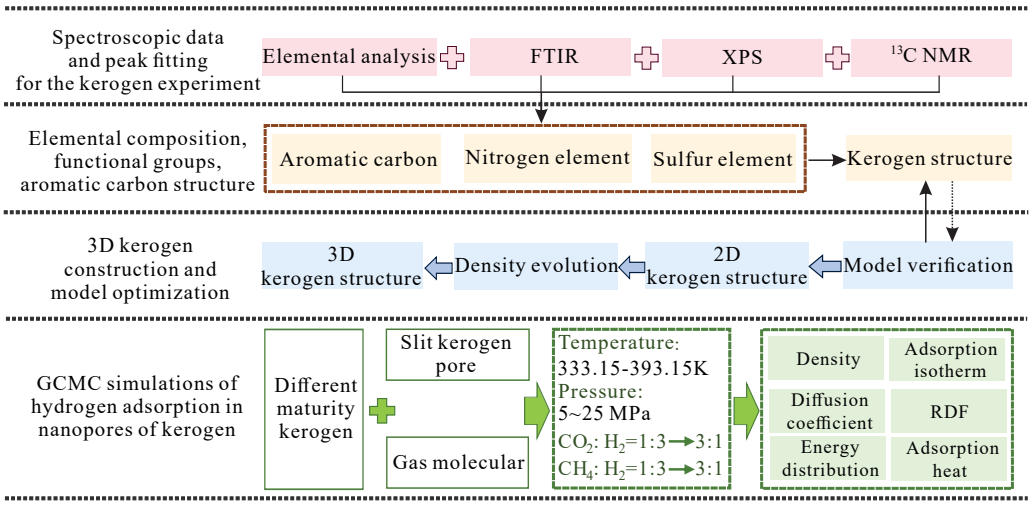



**Fig. 1**. Workflow for kerogen molecular reconstruction and the study of $CO_2$-$H_2$ and $CH_4$-$H_2$ adsorption.

densities in previous studies (Liu et al., 2021) (Fig. 2). During adsorption simulations, the kerogen framework was kept rigid and temperature was controlled using the Nosé thermostat. Slit pores with a spacing of 50 Å and periodic boundaries were used to represent nanopore confinement (Sun et al., 2018). The competitive adsorption of methane/hydrogen and carbon dioxide/hydrogen mixtures was subjected to Grand Canonical Monte Carlo simulations, followed by molecular dynamics analysis. Van der Waals and electrostatic interactions were calculated using atom-based and Ewald methods, respectively, with a cutoff distance of 1.5 nm. Adsorption isotherms were obtained at 21 pressure points up to 20 MPa, with $2 \times 10^7$ Monte Carlo steps per point, including equal equilibration and production stages.

#### 2.4.3 Analytical methods

To quantitatively evaluate the adsorption and transport mechanisms of the $CO_2$/$CH_4$/$H_2$ mixture, several key parameters were determined. The absolute and excess adsorption capacities were calculated to characterize gas uptake within the kerogen matrix. Radial distribution function (RDF) analysis was conducted to characterize local structural ordering and gas-kerogen interaction distances. Interaction strength was evaluated using the isosteric heat of adsorption ($Q_{st}$), which reflects the energetic heterogeneity of the system. The detailed equations for adsorption isotherms, RDF, $Q_{st}$, and MSD are provided in the Supplementary file.

## 3. Results

### 3.1 Organic geochemistry characteristics

Rock pyrolysis indicated that the shale organic matter samples (GU5 and L10) exhibit a maximum pyrolysis temperature ($T_{max}$) of 433 °C, soluble hydrocarbons ($S_1$) lower 0.02 mg/g, pyrolyzable hydrocarbons from organic matter ($S_2$) of 0.07 mg/g, and hydrocarbon potential of 0.0794 mg/g, demonstrating favorable pyrolytic hydrocarbon generation characteristics (Table S2).

### 3.2 Spectroscopic analysis of kerogen structure

#### 3.2.1 Raman spectroscopy analysis

To determine kerogen maturity, Raman spectroscopy experiments were conducted. Multiple-point measurements were performed to mitigate OM heterogeneity. The curves within the Raman shift range of 1,000-2,000 $cm^{-1}$ were fitted, and the maturity of OM in samples was calculated using previously established methods (Fig. S1). The maturities of the samples were 2.89% and 3.24%, respectively, belonging to high to overmature stages. Meanwhile, a low-amplitude protrusion appeared at the position of the S2 peak, indicating that the degree of carbonization of OM was not obvious (Wang et al., 2022).

#### 3.2.2 XRD analysis

To evaluate mineral removal after kerogen isolation and to characterize the structural ordering of organic matter, X-ray diffraction analysis was performed. After separation, mineral peaks in the Longmaxi shale were largely removed, and the isolated kerogen showed a smoother OM dominated pattern with minor residual mineral peaks (Fig. 3). The XRD patterns of kerogen show two broad peaks at $2\theta = 20°$-$30°$ and $2\theta = 40°$-$50°$, corresponding to the 002 plane and 100 peak of graphitic microcrystalline structures (Liu et al., 2021; Liang et al., 2024), respectively. The XRD curve indicates that the 002-crystal plane develops significantly higher than the 001 plane. Compared with GU5, L10 exhibits a narrower peak width and higher intensity, suggesting stronger aromatic stacking and carbonization.

#### 3.2.3 XPS analysis

A wide-scan XPS analysis of kerogen revealed the relative contents of four elements: carbon, oxygen, nitrogen, and sulfur. The results showed that carbon accounts for the largest proportion, exceeding 80% (Fig. 4). Oxygen follows with a content of approximately 12%, while nitrogen and sulfur each account for less than 5% (Table S3). Notably, a relatively high percentage of elements such as F are also evident, likely cau-

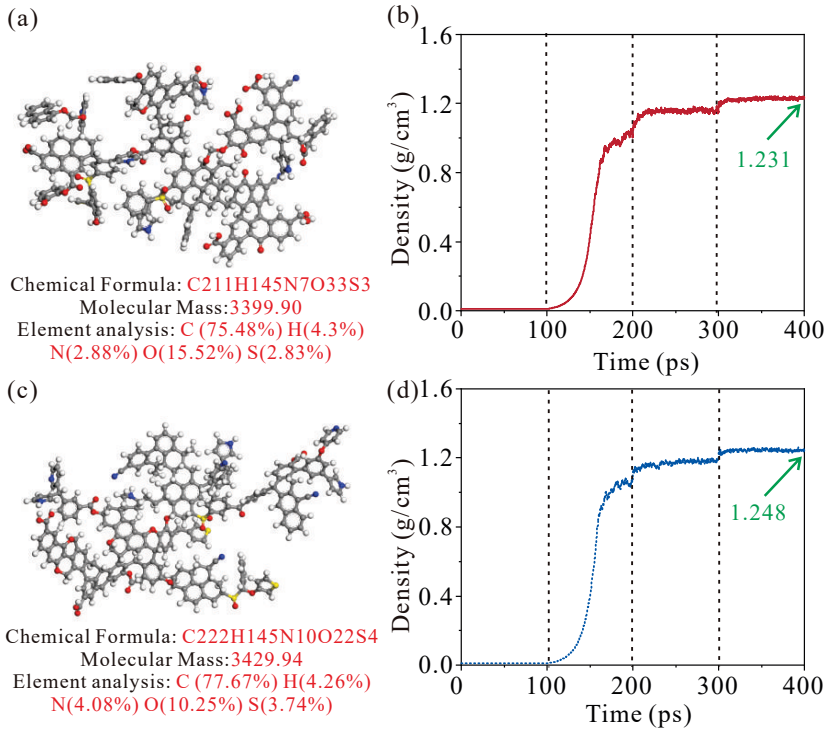



**Fig. 2**. Molecular structures, periodic cell models, and density evolution of kerogen with different thermal maturities: (a)-(b) GU5 kerogen and (c)-(d) L10 kerogen

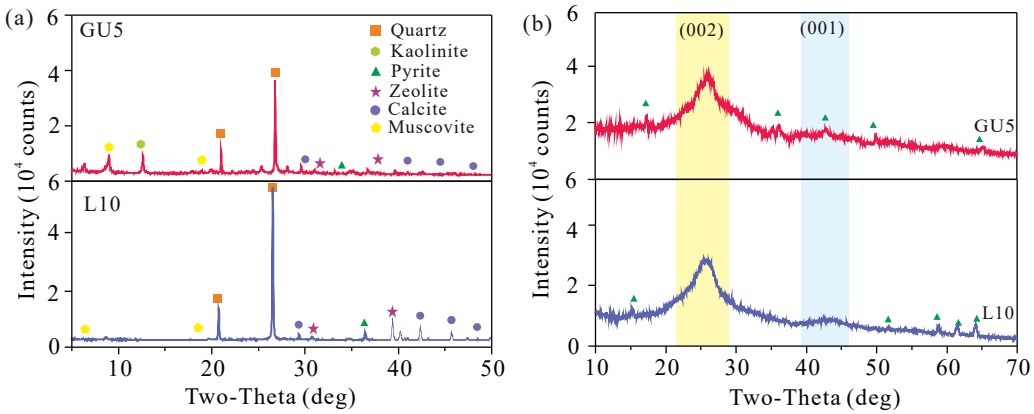



**Fig. 3**. XRD characteristics of shale samples and their corresponding kerogen contents: (a) XRD spectrum of shale and (b) XRD spectrum of kerogen corresponding to shale extraction.

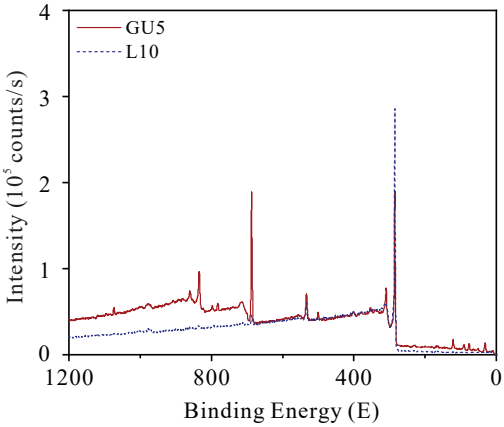



**Fig. 4**. Wide-spectrum XPS of kerogen at different maturity levels.

sed by residual substances from the kerogen preparation process.

X-ray photoelectron spectroscopy peak fitting of C1s, O1s, N1s, and S2p spectra was conducted to determine the chemical states and relative contents of major elements in kerogen (Tian et al., 2019; Hou et al., 2023) (Fig. 4). The C1s spectra (Table 1) showed that carbon is mainly present as aliphatic and aromatic carbon, followed by carbon bonded to ether or hydroxyl groups, with minor contributions from carbonyl and carboxyl carbon (Fig. 5(a)). Oxygen occurs mainly as carbon-oxygen single bonds, carbonyl oxygen, and carboxyl oxygen (Fig. 5(c)). Compared with C1s and O1s, the N1s and S2p signals are much weaker, indicating low nitrogen and trace sulfur contents. Nitrogen is dominated by pyridinic, quaternary

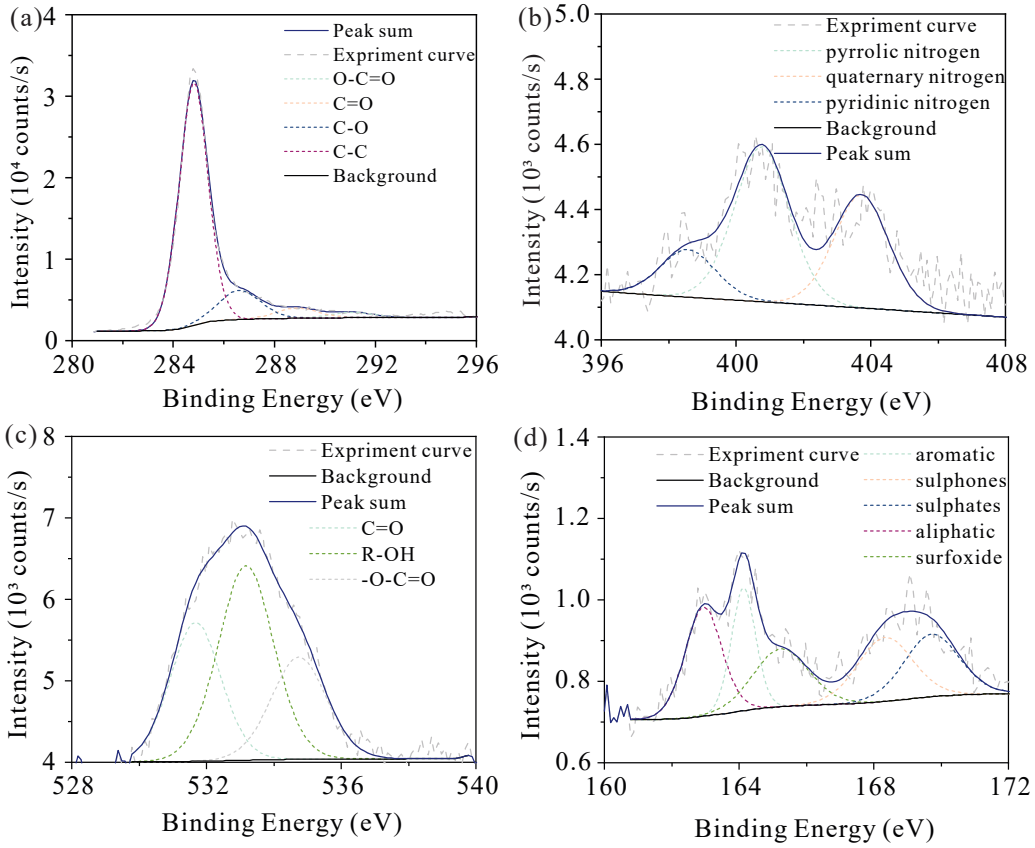



**Fig. 5**. High-resolution XPS spectra of the main elements C, N, O, and S in kerogen and the peak fitting characteristics of different elements: (a) C1s, (b) N1s, (c) O1s, and (d) S2p.

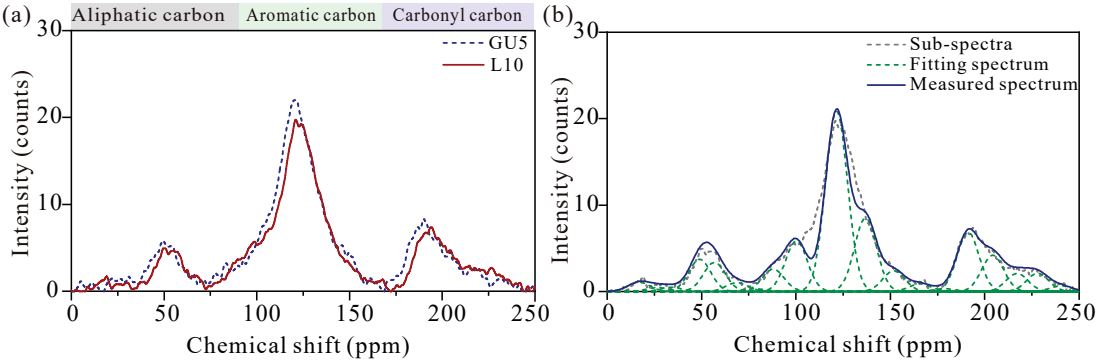



**Fig. 6**. $^{13}C$ NMR curve of kerogen and its peak fitting characteristics: (a) Carbon-type assignments and representative chemical shifts, and (b) fitted sub-spectra of the measured spectrum.

and pyrrolic nitrogen (Fig. 5(b)), whereas sulfur mainly occurs as aromatic/aliphatic sulfur, sulfone and sulfoxide species (Fig. 5(d)).

### *3.2.4 Solid-state $^{13}C$ NMR data analysis*

Solid-state $^{13}C$ NMR was employed to characterize the carbon framework of Longmaxi kerogen. As shown in Fig. 6(a), the spectra can be divided into three regions: aliphatic carbon (0-90 ppm), aromatic carbon (90-165 ppm), and carbonyl carbon (165-220 ppm).

Spectral deconvolution was conducted to quantify the proportions of different carbon types (Fig. 6(b)). Aromatic carbon accounts for an average of 59.92%, whereas aliphatic carbon represents 16.48%. In the aliphatic region, the dominant 45-60 ppm peak indicates abundant oxygen-bearing aliphatic carbons and methylene groups (Table 2). Kerogen from the Longmaxi Formation exhibits a high aromaticity, exceeding 60%, including multiple naphthalene, phenanthrene, and $2 \times 2$ aromatic structures. In the aromatic region (90-165 ppm), oxygenated aromatic carbons are dominant, accounting for over 20%. These are followed by protonated aromatic carbons, with a content of more than 15%, while the content of bridging aromatic carbons is maintained at 10%.

**Table 1**. Statistical table of different valence states of the main C, N, O, and S elements in kerogen.

| Element | Functional group | GU5 | | L10 | |
|---|---|---|---|---|---|
| | | Binding energy | Content (%) | Binding energy | Content (%) |
| C1s | C-C, C=C, C-H | 284.8 | 78.93 | 284.8 | 77.10 |
| | C-O | 286.6 | 13.69 | 286.7 | 12.41 |
| | C=O | 288.9 | 4.83 | 289.1 | 5.95 |
| | COOH | 291.1 | 2.54 | 291.4 | 4.54 |
| N1s | Pyridine | 398.6 | 15.05 | 398.5 | 25.49 |
| | Pyrrole | 400.8 | 49.14 | 400.8 | 52.50 |
| | Amine | 403.7 | 35.82 | 403.6 | 22.00 |
| O1s | C-O | 531.7 | 30.09 | 531.1 | 32.21 |
| | O-C-O, C=O | 533.2 | 45.85 | 532.5 | 46.74 |
| | O-C=O | 534.7 | 24.06 | 534.0 | 21.05 |
| S2p | Aliphatic sulfur | 162.9 | 23.42 | 162.8 | 7.19 |
| | Aromatic sulfur | 164.1 | 17.46 | 165.0 | 21.09 |
| | Sulfoxides | 165.2 | 18.60 | 164.0 | 23.32 |
| | Sulphones | 168.3 | 20.51 | 168.2 | 32.04 |
| | Sulphates | 169.7 | 20.01 | 169.4 | 16.37 |

#### 3.2.5 FTIR analysis

Following previous studies, the absorbance peaks were assigned to identify the functional-group characteristics of kerogen (Chen et al., 2015; Oye, 2022; Gomez-Neita et al., 2025). The two kerogen samples show broadly similar FTIR features (Fig. 7). The bands at 700-900 and 1,550-1,650 $cm^{-1}$ are attributed to aromatic C–H out-of-plane bending and aromatic C=C skeletal vibrations, respectively. The 1,100-1,300 $cm^{-1}$ interval represents C–O vibrations from ether and hydroxyl groups, while the 1,710 $cm^{-1}$ is assigned to carbonyl C=O stretching, the 2,800-3,000 $cm^{-1}$ range is associated with aliphatic methyl and methylene groups, and the band at 3,450 $cm^{-1}$ corresponds to hydroxyl groups. These FTIR-derived structural features are consistent with the $^{13}C$ NMR results. The functional-group assignments for different peak intensities are listed in Table S4.

To further quantify the functional group characteristics, peak fitting was conducted for the FTIR regions associated with aromatic carbon, oxygen-containing groups, and aliphatic carbon (Fig. S2), including 450-950, 900-1,500, 1,500-1,800, and 2,800-3,000 $cm^{-1}$, following previous studies (Gomez-Neita et al., 2025). Sub-peak assignments and relative contents were determined based on published references (Gomez-Neita et al., 2025). The calculated aromatic carbon ratio (I) and degree of condensation of GU5 are significantly higher than those of L10, indicating clear maturity-related differences in the chemical structure of kerogen (Table S5).

### 3.3 Pore structure characteristic of kerogen

Low-pressure gas adsorption analyses were applied to assess maturity-related differences in kerogen micropores and mesopores. GU5 shows higher carbon dioxide adsorption than L10 at $P/P_o < 0.03$, due to better-developed microporosity (Fig. 8(a)). Its micropores are mainly distributed at 0.45-0.65 nm, accompanied by a minor peak at 0.75-0.85 nm, and exhibit higher pore volume and surface area than L10 (Figs. 8(b) and 8(c)). GU5 displays an overall higher pore volume intensity across this range. Correspondingly, the micropore specific surface area distribution of GU5 is also markedly higher than that of L10. Figs. 8(d)-8(f) present the $N_2$ adsorption results for mesopores. GU5 exhibits higher $N_2$ adsorption capacity than L10. The mesopore pore volume and surface area distributions (Figs. 8(e) and 8(f)) further indicate that GU5 consistently exceeds L10 within the 1-10 nm pore size range. These results suggest that GU5 has stronger micropore adsorption capacity and more developed mesopores than L10.

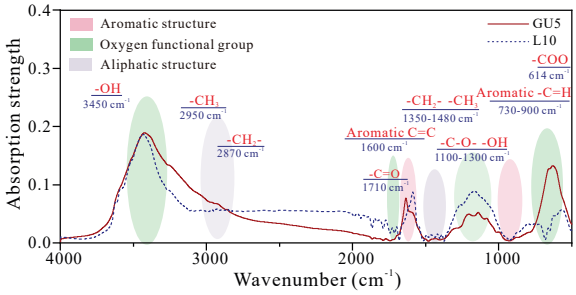



**Fig. 7**. FTIR spectrum curve of kerogen and corresponding functional groups.

**Table 2**. $^{13}$C NMR chemical shift and corresponding functional group characteristics.

| Carbon assignment (Symbol) | Ratio (%) | |
|---|---|---|
| | GU5 | L10 |
| Aliphatic methyl ($f_{al\text{-}M}$) | 1.03 | 0.53 |
| Aromatic methyl ($f_{al\text{-}A}$) | 0.27 | 0.77 |
| Methylene ($f_{al\text{-}H}$) | 1.33 | 0.88 |
| Methine, quaternary ($f_{al\text{-}D}$) | 5.80 | 4.38 |
| O-methylene ($f_{al\text{-}O}$) | 2.46 | 2.03 |
| O-methine ($f_{al\text{-}O}$) | 2.30 | 3.73 |
| O-aliphatic ($f_{al\text{-}O}$) | 3.56 | 3.89 |
| O-aromatic ring ($f_{ar\text{-}A}$) | 23.29 | 20.24 |
| Protonated aromatic ($f_{ar\text{-}H}$) | 15.39 | 17.62 |
| Bridged aromatic ($f_{ar\text{-}B}$) | 8.03 | 7.26 |
| Branched aromatic ($f_{ar\text{-}C}$) | 9.52 | 11.02 |
| Oxygen-aromatic ($f_{ar\text{-}O}$) | 3.57 | 3.89 |
| Carboxyl ($f_{a\text{-}C}$) | 7.10 | 6.92 |
| Carbonyl ($f_{a\text{-}O}$) | 12.80 | 13.42 |

## 3.4 2D/3D kerogen structure reconstruction and validation

The structural parameters of Longmaxi kerogen were determined using elemental analysis, FTIR, solid-state $^{13}$C NMR, and XPS. XPS was used to constrain the relative proportions of $N^-$ and S-containing functional groups, while elemental analysis provided the basic C and O contents. The carbon skeleton, including aromatic, aliphatic, carboxyl, and carbonyl carbons, was quantified mainly from the $^{13}$C NMR results. Oxygen-containing structures, such as C–O, C=O, and O–C=O groups, were further constrained by integrating XPS and NMR data. Based on these experimental constraints, the 2D kerogen molecular models were constructed and calibrated using MestReNova by comparing the simulated and the experimental NMR characteristics. The structures were iteratively adjusted until reasonable agreement was reached with the experimental parameters, and the final kerogen models are shown in Fig. S3.

## 3.5 Adsorption of $CH_4/H_2$ and $CO_2/H_2$ in slit nanopores

### 3.5.1 Mixed gas adsorption analysis

OM is characterized by a rich matrix of nanopores and significant development of slit-like OM pores. To assess maturity-related variations in gas storage, $CH_4/H_2$ and $CO_2/H_2$ adsorption in kerogen slit models was examined under varying pressures, temperatures and gas compositions (Figs. 9 and S4). The total uptake can be observed to increase with pressure. $CH_4$ and $CO_2$ adsorption rises rapidly at low pressure and then gradually levels off, whereas $H_2$ shows an approximately linear increase. At a 1 : 1 molar ratio, $CO_2$ has the greatest adsorption capacity, reflecting its strongest affinity for the kerogen matrix (Figs. 9(b) and 9(e)). Owing to its small molecular size and weak kerogen interaction, $H_2$ exhibits negative excess adsorption at high pressure, as bulk-phase density increases more rapidly than adsorbed-phase density. This may reflect the weak physisorption of hydrogen, as adsorption becomes less favorable at a high molecular coverage (Al-Harbi et al., 2023). In this study, with increasing pressure, the excess adsorption amount of some $H_2$ becomes negative, which may be related to this phenomenon. Increasing the $H_2$ content enhances its absolute adsorption, but $CO_2$-rich mixtures strongly suppress $H_2$ adsorption through the competitive occupation of adsorption sites. GU5 consistently shows higher adsorption capacities than L10, particularly for $CH_4$ and $CO_2$ at high pressures, indicating that kerogen maturity strongly controls mixed-gas adsorption (Fig. S4). As for temperature, it exerts a weaker influence than pressure and maturity.

### 3.5.2 Adsorption selectivity analysis

To better define the differences in adsorption capacity between $CO_2/H_2$ and $CH_4/H_2$ systems, the adsorption selectivity coefficient of component $i$ over $j$ ($S_{i/j}$) was calculated under varying pressures, temperatures and mixing ratios. For this operation, the selectivity was defined as:

$$S_{i/j} = \frac{\left(\frac{x_i}{x_j}\right)_{ads}}{\left(\frac{x_i}{x_j}\right)_{bulk}} \tag{1}$$

where $x_i$ and $x_j$ represent the mole fractions of components $i$ and $j$ in the adsorbed phase, respectively, while $y_i$ and $y_j$ denote their corresponding mole fractions in the bulk phase (free gas). For the $CH_4/H_2$ system, the results show that the selectivity coefficient decreases progressively with increasing pressure (Fig. 10). At a constant temperature, selectivity is significantly higher at lower pressure. Furthermore, mixtures with higher $H_2$ content generally exhibit higher selectivity at low pressures. However, as pressure increases toward 15 MPa, the selectivity coefficients for all ratios converge to approximately

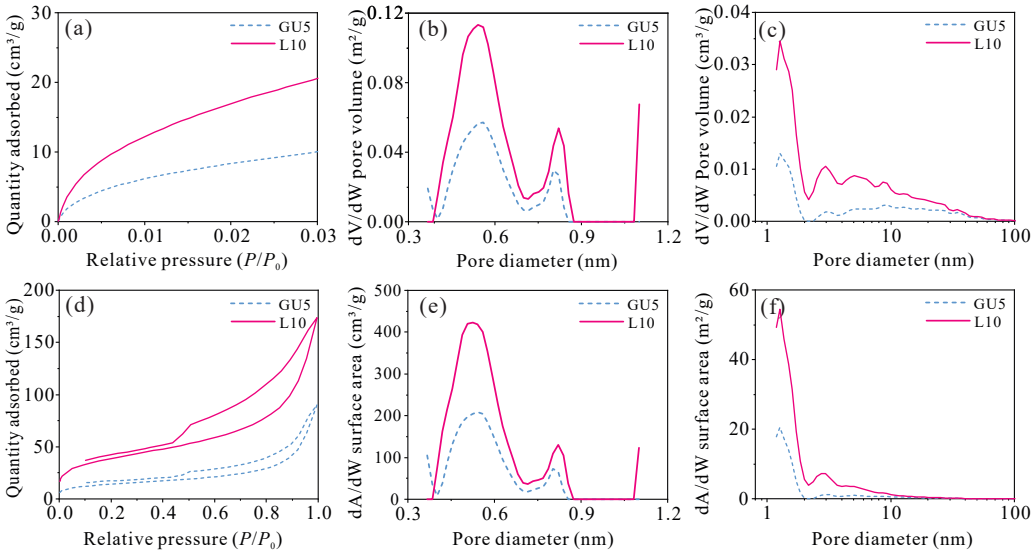



**Fig. 8**. Gas adsorption and pore structure characteristics of kerogen: (a)-(c) $CO_2$ adsorption for micropore characteristics; (d)-(f) $N_2$ adsorption for mesopore characteristics.

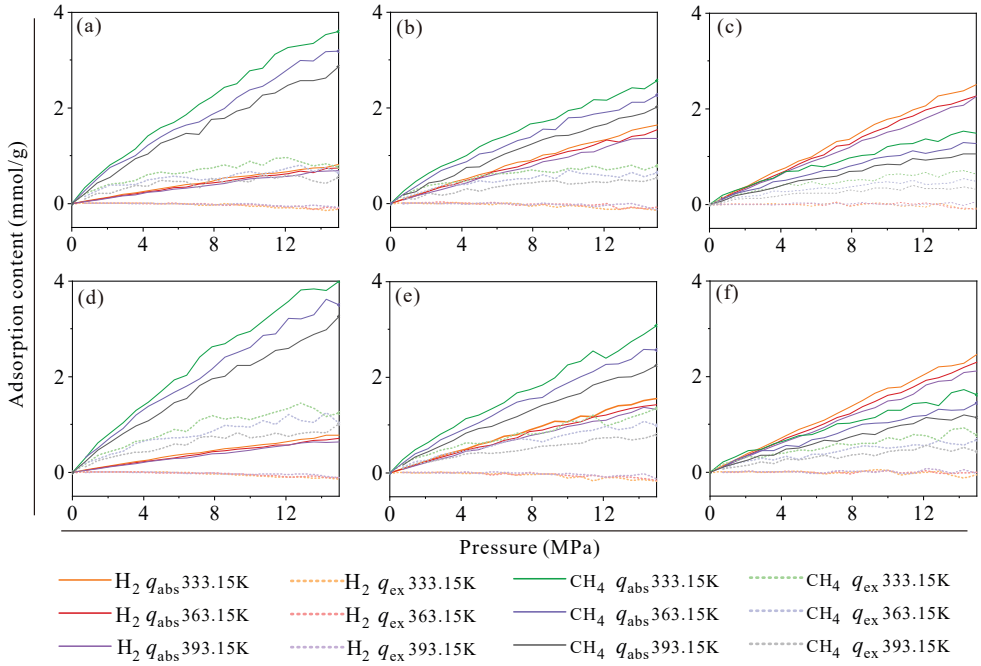



**Fig. 9**. Mixed gas adsorption capacity of kerogen slit pores with different pore proportions under varying pressures and temperatures. (a)-(c) GU5 kerogen slit pore adsorption capacity with $CH_4$:$H_2$ at 3:1 to 1:3 and (d)-(f) L10 kerogen slit pore adsorption capacity with $CH_4$:$H_2$ at 3:1 to 1:3.

1.5 (Figs. 10(a)-10(c)). In terms of thermal maturity, although the adsorption isotherms appear similar across samples, the over-mature kerogen consistently exhibits higher selectivity coefficients compared to the high-maturity organic matter. In contrast, the $CO_2/H_2$ system exhibits substantially higher selectivity, exceeding 5.0 at low pressures. This highlights the significantly stronger intermolecular interactions and superior surface affinity of $CO_2$ compared to $H_2$ (Figs. 10(d)-10(f)). As pressure increases, the selectivity coefficient gradually decreases, remaining around 5.0 at 15 MPa. Unlike the $CH_4/H_2$ system, the impact of kerogen maturity on $CO_2/H_2$ selectivity is less pronounced. Notably, at low temperatures and high pressures, some selectivity values appear anomalously high (Figs. 10(d) and 10(f)). This phenomenon likely stems from the exclusion of weakly adsorbed $H_2$ molecules from the adsorbed phase; as the adsorbed-phase density of $H_2$ falls below its bulk-phase density, more $H_2$ molecules are displaced into the free gas phase, thereby artificially inflating the selectivity of the more strongly adsorbed species.

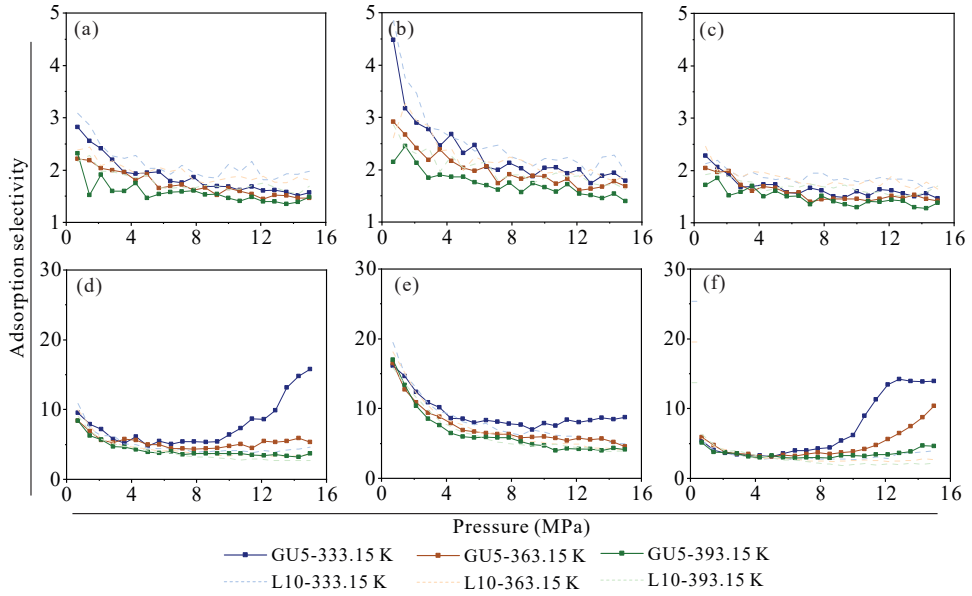



**Fig. 10**. Adsorption selectivity of mixed gases under different pressures and temperatures: (a) $CH_4/H_2$ = 1:1; (b) $CH_4/H_2$ = 1:3, (c) $CH_4/H_2$ = 3:1, (d) $CO_2/H_2$ = 1:1, (e) $CO_2/H_2$ = 1:3 and (f) $CO_2/H_2$ = 3:1.

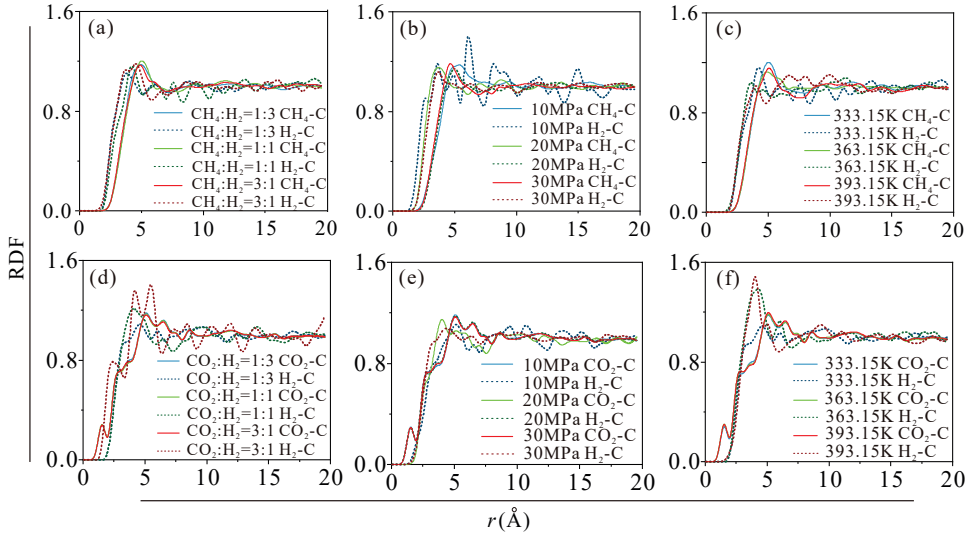



**Fig. 11**. RDF between gas molecules and kerogen carbon atoms in GU5 under different gas compositions, pressures and temperatures: (a) $CH_4/H_2$ ratio, (b) pressure for $CH_4$-carbon RDF, (c) temperature for $CH_4$-carbon RDF, (d) $CO_2/H_2$ ratio, (e) pressure for $CO_2$-carbon RDF and (f) temperature for $CO_2$-carbon RDF.

## 4. Discussion

### *4.1 Microscopic configuration and distribution under competitive adsorption*

RDF analysis was employed to systematically compare the interactions between gas molecules and carbon atoms in kerogen under different temperature and pressure conditions, as well as for different $CO_2/H_2$ and $CH_4/H_2$ mixing ratios (Fig. 11 and Fig. S5). The RDF curves show that both $CH_4$ and $CO_2$ exhibit pronounced first peaks at distances of approximately 3-5 Å from the kerogen carbon atoms, indicating the preferential enrichment of these gas molecules near the surface of OM nanopores (Zhang et al., 2023) (Figs. 11(a)-11(c)). This indicates that gas occurrence in kerogen nanopores is mainly controlled by interfacial interactions, rather than by simple pore-filling effects. Compared with $CH_4$, $CO_2$ generally displays a higher first-peak intensity and more pronounced oscillatory behavior (Figs. 11(d)-11(f)), indicating a stronger affinity for the carbon framework and a higher degree of local ordering. This difference is likely related to the stronger quadrupole moment and higher polarizability of $CO_2$ relative to $CH_4$ (Alanazi et al., 2024).

Further comparison between GU5 and L10 demonstrated that pore structure plays a critical role in controlling the local distribution behavior of gas molecules (Fig. 11 and Fig. S5). The RDF curves of GU5 are generally smoother

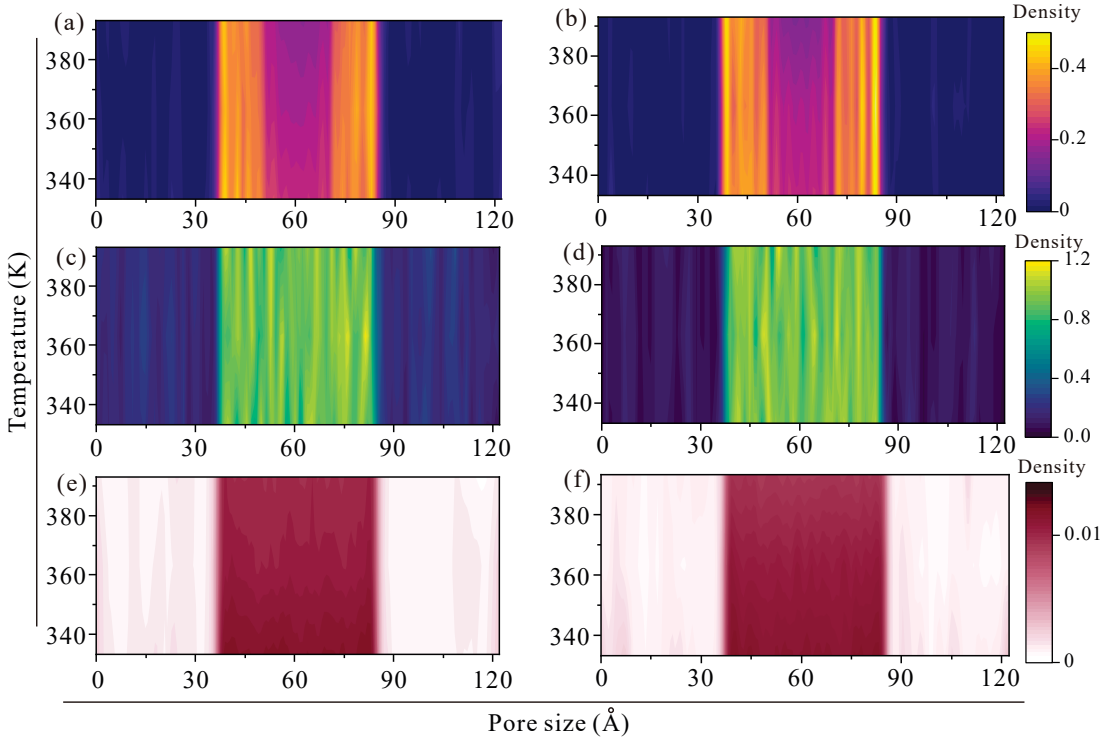



**Fig. 12**. (a)-(b) $CH_4$ density profiles in GU5 and L10 kerogen, respectively, (c)-(d) $CO_2$ density profiles in GU5 and L10 kerogen, respectively, and (e)-(f) $H_2$ density profiles in GU5 and L10 kerogen, respectively.

and exhibit weaker fluctuations (Fig. 11), suggesting that its better-developed pore network provides more space for gas molecules. In contrast, L10 shows sharper peaks and stronger oscillations, particularly in the $CO_2$ related systems (Fig. S5), indicating that under poorer pore-structure conditions, gas molecules are more likely to accumulate near the kerogen pore surface. Therefore, compared with changes in gas composition, pore structure exerts a more significant control on gas distribution behavior. The gas mixing ratio and pressure have limited effects on RDF peak positions, indicating relatively stable adsorption distances between gas molecules and the carbon surface. Pressure mainly changes local packing density and ordering, whereas higher temperature weakens the first RDF peak, reflecting reduced interfacial adsorption and local ordering. Overall, kerogen maturity affects gas occurrence not only by changing pore volume but also by modifying pore connectivity, confinement, and interfacial properties within the nanoscale reservoir space.

## 4.2 Adsorption density of slit kerogen pore

### 4.2.1 Single gas adsorption

To clarify the gas occurrence states in kerogen slit pores, the density profiles of $CH_4$, $CO_2$ and $H_2$ were analyzed. Marked differences are observed among the three gases in both GU5 and L10 kerogen models (Fig. 12 and S6). Although all density profiles are symmetric, their distinct gas interactions produce different adsorption behaviors. $CH_4$ forms a pronounced near-surface adsorption layer, with much higher density at the pore surface than at the center, indicating surface-dominated adsorption (Figs. 12(a)-12(d)). Increasing temperature weakens this adsorption layer, whereas increasing pressure enhances $CH_4$ enrichment near the kerogen pore surface, consistent with previous studies on methane adsorption in organic slit pores (Hou et al., 2023). Compared with $CH_4$, $CO_2$ shows a much higher overall density and a smaller density contrast between the surface and pore middle (Figs. 12(c)-12(d)), indicating a shift from surface adsorption toward pore filling. This reflects the stronger interaction between $CO_2$ and kerogen, which promotes high in-pore density. In contrast, $H_2$ exhibits the lowest density and no distinct near-surface adsorption layer (Figs. 12(e)-12(f)), consistent with a previous study (Sikiru et al., 2024), suggesting that $H_2$ adsorption on shale/mineral surfaces is weak physical adsorption with low energy and free distribution in the pore center (Al-Harbi et al., 2023; Chen et al., 2023). Higher pressure enhances $H_2$-surface and $H_2$-$H_2$ interactions, while increasing temperature weakens the adsorption layer, consistent with previous $H_2$ adsorption studies in kaolinite and silica pores (Al-Harbi et al., 2025).

The difference between GU5 and L10 is mainly expressed in the near-kerogen adsorption density (Fig. 12 and Fig. S6). $CH_4$ and $CO_2$ generally show higher kerogen surface-associated densities in L10 than in GU5, indicating that stronger confinement in L10 favors the accumulation of dominant adsorbed components near the kerogen pore surface. By contrast, the larger pore space of GU5 results in a more uniform gas distribution. Overall, gas occurrence in kerogen nanopores is jointly controlled by gas properties and pore confinement. $CH_4$ is characterized by near-kerogen surface

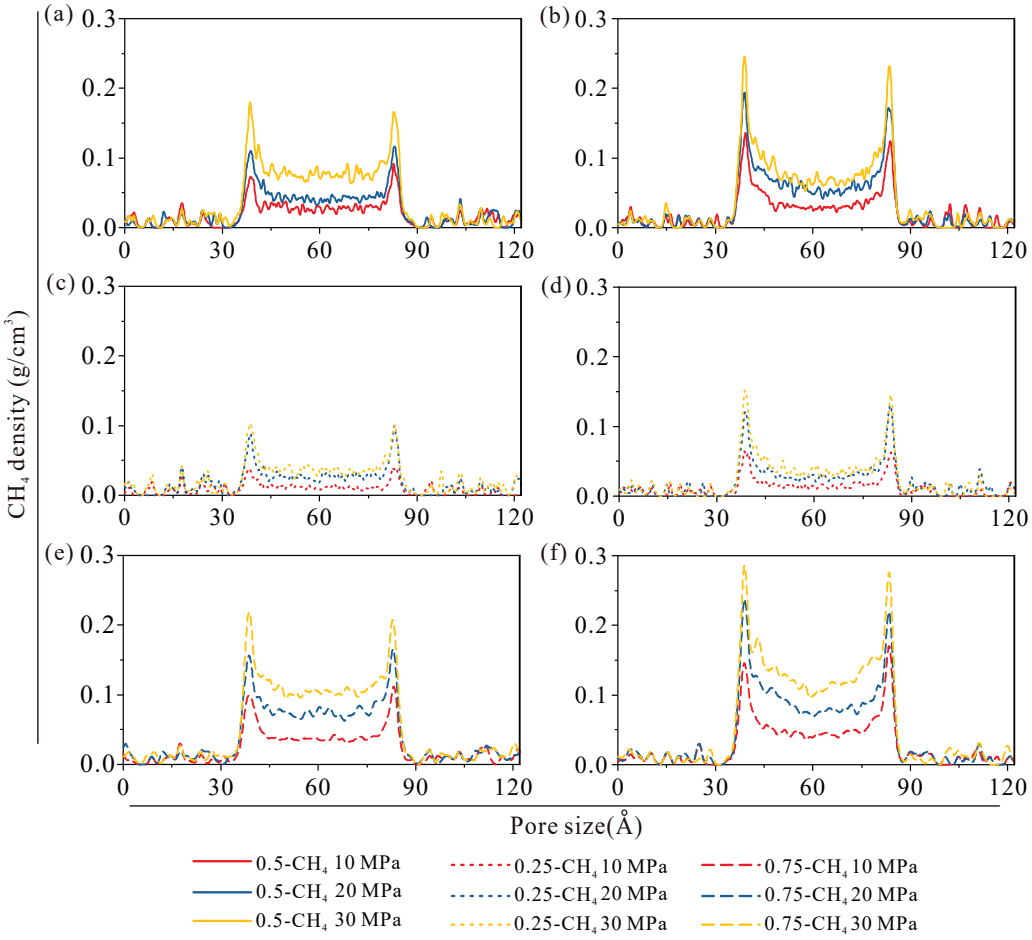



**Fig. 13**. Adsorption density distributions of $CH_4$ density profiles in kerogen slit pores at different mixing ratios and pressures: (a), (c), (e) GU5 and (b), (d), (f) L10 for $CH_4/H_2$ ratios of 1:1, 1:3 and 3:1, respectively.

layered adsorption, while $CO_2$ shows a stronger pore-filling tendency, and $H_2$ remains a weakly adsorbed component. In general, increasing temperature weakens surface adsorption, whereas increasing pressure enhances gas enrichment in kerogen pores.

### *4.2.2 Mixed gas adsorption*

During competitive adsorption, $CH_4$ and $CO_2$ are preferentially enriched near the kerogen surface, whereas hydrogen remains mainly bulk-like in the pore space, indicating pronounced interfacial competition controlled by adsorbate–surface interactions (Zhang et al., 2024a). In contrast, $H_2$ shows only a minor density difference between the kerogen pore surface and pore center, without forming a distinct high-density adsorption layer, which indicates that it mainly occurs in the pore space in a bulk-like state. In the $CH_4/H_2$ system, $CH_4$ dominates the adsorption-layer structure by occupying favorable surface sites (Fig. 13 and Fig. S7), consistent with previous observations in kaolinite slit pores where $CH_4$ showed stronger pore-wall interactions than hydrogen (Zhang et al., 2023). Increasing pressure continuously enhances methane density near the kerogen surface, while the central pore density changes only slightly (Fig. 13), indicating that pressurization mainly promotes $CH_4$ adsorption at the kerogen surface (Sikiru et al., 2024). An increase in $CH_4$ fraction further enhances its surface adsorption density, suggesting that the mixing ratio directly controls the amount of $CH_4$ in the adsorbed phase. As shown in Fig. S7, increasing temperature generally causes a slight decrease in $CH_4$ surface adsorption density, consistent with previous studies (Chen et al., 2026). However, this effect is not obvious at low $CH_4$ fractions, implying that temperature has a weaker influence on $CH_4$ spatial distribution than pressure and gas composition. Compared with GU5, L10 generally exhibits higher near-surface methane density, indicating stronger confinement and a more compact adsorption layer in overmature kerogen. In contrast, hydrogen exhibits limited maturity-dependent variation. The above results suggest that maturity mainly controls strongly adsorbed gases by altering pore confinement and interfacial adsorption sites, while its effect on weakly adsorbed hydrogen is limited.

For the $CO_2/H_2$ system, $CO_2$ shows much higher adsorption density near the pore walls than in the pore center, often by several times (Fig. 14 and Fig. S8), indicating a much stronger surface affinity under competitive adsorption conditions (Alanazi et al., 2024). With increasing pressure, the near-wall adsorption density of $CO_2$ increases continuously, whereas the bulk-phase density changes only slightly, suggest-

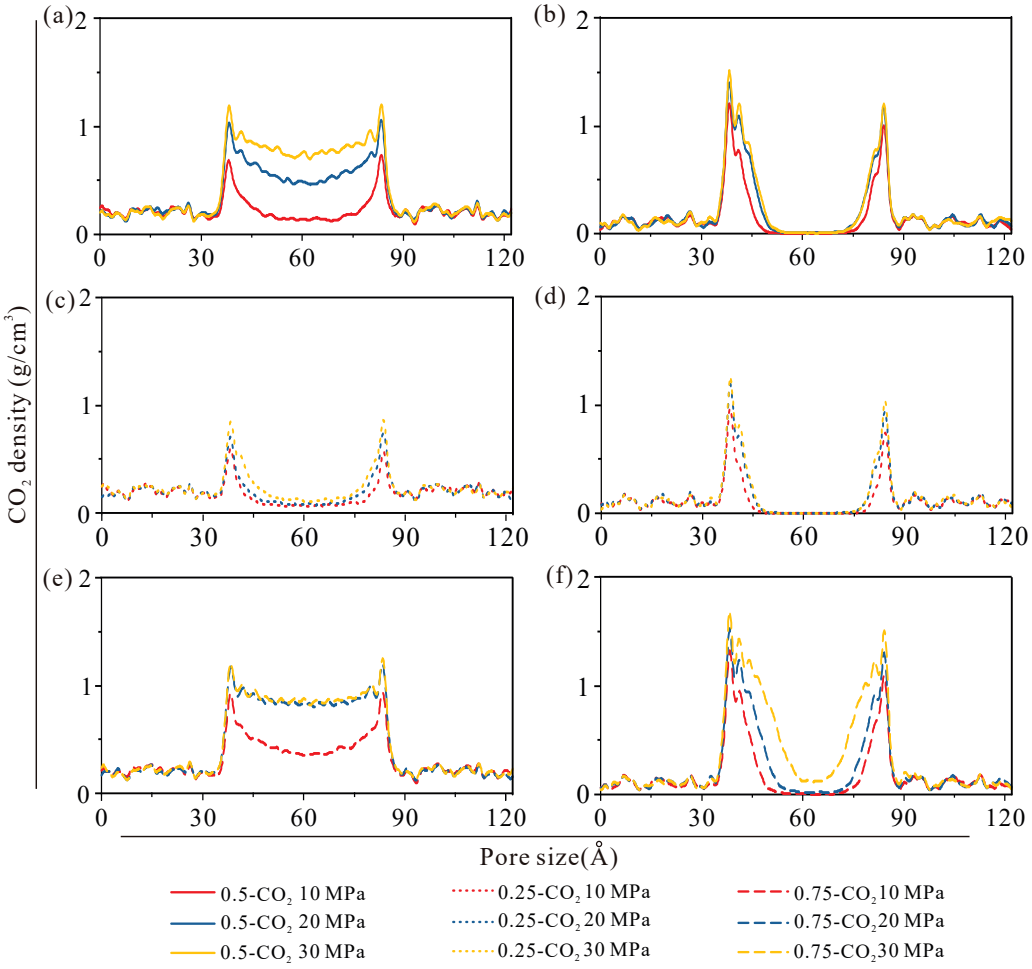



**Fig. 14**. Adsorption density distributions of $CO_2/H_2$ density profiles in kerogen slit pores at different mixing ratios and pressures: (a), (c), (e) GU5 and (b), (d), (f) L10 for $CO_2/H_2$ ratios of 1:1, 1:3 and 3:1, respectively.

ing that pressurization mainly promotes $CO_2$ accumulation at adsorption sites. A higher $CO_2$ fraction further enhances its surface adsorption density, confirming its stronger competitive advantage for available adsorption sites (Zhang et al., 2024a; Al-Harbi et al., 2025). Fig. S8 further shows that increasing temperature slightly reduces the near-wall adsorption density of $CO_2$, indicating that enhanced thermal motion weakens its adsorption stability. Similar to the $CH_4/H_2$ system, $H_2$ in the $CO_2/H_2$ mixture shows little difference between surface and bulk densities, remaining in a weakly adsorbed or free-distribution state. In addition, $CO_2$ exhibits higher near-wall adsorption density in L10 than in GU5, and this maturity-related difference is more pronounced than that in the $CH_4/H_2$ system, indicating that stronger confinement and surface interactions further enhance $CO_2$ adsorption on kerogen.

Overall, gas occurrence in kerogen slit pores is jointly controlled by adsorption affinity, interfacial competition, and pore confinement. Both $CH_4$ and $CO_2$ show much stronger surface enrichment than $H_2$, with $CO_2$ displaying the strongest competitive advantage. Pressure rise mainly enhances the accumulation of the dominant component near the pore walls (Fig. 14), whereas temperature rise slightly weakens its near-wall adsorption stability (Fig. S8). Structural differences between GU5 and L10 further amplify this competitive effect, making L10 more favorable for the formation of a high-density surface adsorption layer.

### 4.3 Interaction energy of $CH_4/H_2$ and $CO_2/H_2$ adsorption

In the $CH_4/H_2$ system, gas-kerogen interactions are dominated by van der Waals forces, while electrostatic contributions are negligible (Figs. 15(a)-15(c) and Fig. S9), mainly because $CH_4$ and $H_2$ are non-polar molecules. Higher pressure enhances near-surface gas enrichment and strengthens van der Waals interactions (Fig. S9), whereas higher temperature and increasing $H_2$ fraction weaken the overall interaction. In contrast, the $CO_2/H_2$ system shows stronger electrostatic contributions due to the quadrupole moment of $CO_2$ and its interaction with polar functional groups and aromatic structures in kerogen. These interactions are more sensitive to temperature, gas composition, and maturity-related changes in kerogen surface chemistry (Mohammed et al., 2023; Li et al., 2024), indicating that maturity plays a more important role in regulating $CO_2/H_2$ competitive adsorption than $CH_4/H_2$ adsorption. Kerogen maturity has only a limited effect on the van der Waals-dominated $CH_4/H_2$ system, but it more strongly

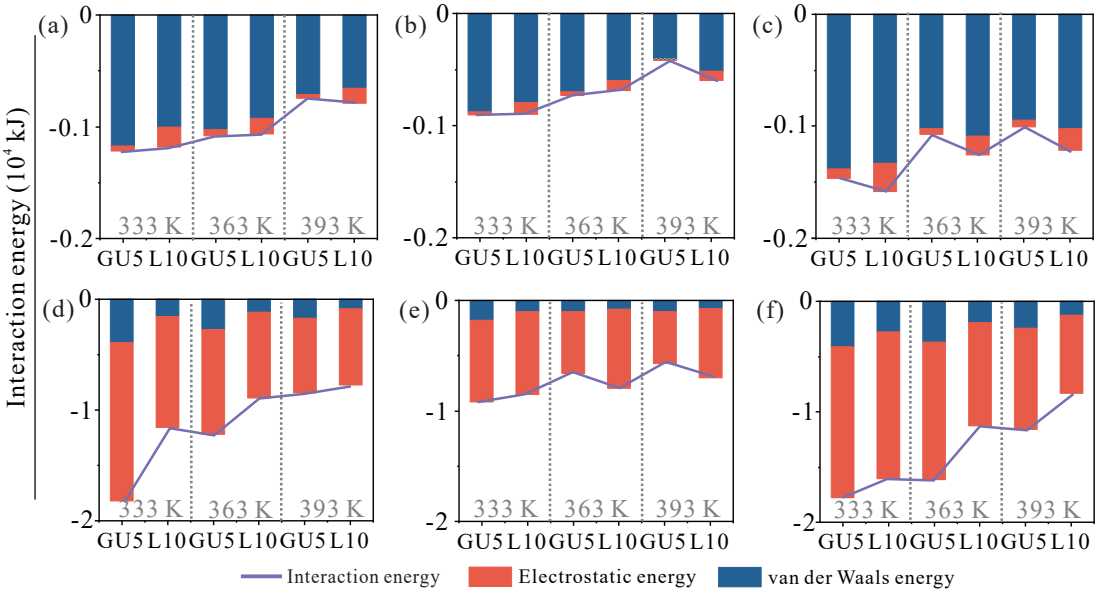



**Fig. 15**. Interaction energy of mixed gas in kerogen slit pores under different pressures. Interaction energy of $CH_4/H_2$ and $CO_2/H_2$ mixtures under different temperatures. (a)-(c) $CH_4/H_2$ at different temperatures and (d)-(f) $CO_2/H_2$ under different temperatures with mixing ratios of 1:1, 1:3 and 3:1, respectively.

regulates $CO_2/H_2$ interactions by altering surface polarity and functional-group heterogeneity, leading to maturity-dependent variations in electrostatic interaction energy (Figs. S9(d)-S9(f)).

The electrostatic potential distributions of the kerogen models and gas molecules were calculated using Dmol3 to qualitatively interpret gas-kerogen interactions (Fig. 16). These results were not used as input parameters for the Grand Canonical Monte Carlo or molecular dynamics simulations, nor for quantitative force-field validation, but served as complementary evidence for visualizing electrostatic heterogeneity (Psarras et al., 2017). Heterogeneous electrostatic potential around aromatic structures and oxygen-containing groups provides favorable sites for quadrupolar carbon dioxide, whereas methane and hydrogen show more uniform electrostatic characteristics. This qualitatively supports the molecular dynamics results and explains the stronger affinity of $CO_2$ for kerogen.

## 4.4 Diffusion coefficient of mixed competitive adsorption

Under competitive mixed-gas adsorption conditions, the diffusion coefficients generally follow the order of $H_2 > CH_4 > CO_2$ (Fig. 17). Owing to its small molecular size and weak interaction with kerogen, hydrogen mainly occurs in a free or weakly adsorbed state and exhibits the highest mobility, implying easier desorption from nanopores and the potential improvement of hydrogen purity during production (Alanazi2024; Sikiru2024). The mean square displacement of $H_2$ increases most rapidly (reaching approximately 24.0 nm2), whereas $CH_4$ and $CO_2$ show lower mobility due to stronger van der Waals and electrostatic interactions with kerogen, respectively (Sikiru2024; Wang2024). $CH_4$ exhibits intermediate diffusivity, mainly governed by van der Waals interactions, whereas $CO_2$ shows the lowest diffusion coefficient due to its stronger electrostatic interaction with kerogen and more stable adsorption configurations.

Increasing temperature generally enhances gas diffusion, particularly for $CH_4$ and $H_2$, indicating that stronger thermal motion helps molecules overcome interfacial constraints and increases effective displacement (Wang et al., 2024). In contrast, the temperature dependence of $CO_2$ is more complex, suggesting that its diffusion is controlled not only by thermal effects but also by strong adsorption configurations (Fig. 17). Increasing pressure generally suppresses diffusion, with the strongest reduction observed for $H_2$, likely because higher pressure increases molecular collisions and reduces the free volume and transport pathways within kerogen pores. By comparison, $CH_4$ and $CO_2$ are less sensitive to pressure because their mobility is already more strongly restricted by interfacial adsorption, consistent with previous studies (Sikiru et al., 2024; Zhang et al., 2024a; Chen et al., 2026).

Gas composition further modulates molecular diffusion by altering competitive adsorption within kerogen nanopores. In the $CH_4/H_2$ system, increasing the $CH_4$ fraction reduces the diffusion coefficients of both $CH_4$ and $H_2$, indicating that $CH_4$ enrichment at the kerogen surface limits molecular mobility. In the $CO_2/H_2$ system, $H_2$ remains strongly dependent on temperature and pressure, whereas $CO_2$ diffusion is relatively insensitive to composition (Fig. 17). Compared with GU5, the stronger confinement and higher adsorption density of L10 restrict methane and carbon dioxide diffusion and reduce the effective transport space of hydrogen. These results indicate that gas diffusion is controlled by gas properties, thermodynamic conditions, composition, and maturity-related pore structure. For underground hydrogen storage, hydrogen diffusivity should be evaluated together with adsorption capacity, because excessive hydrogen mobility may limit storage

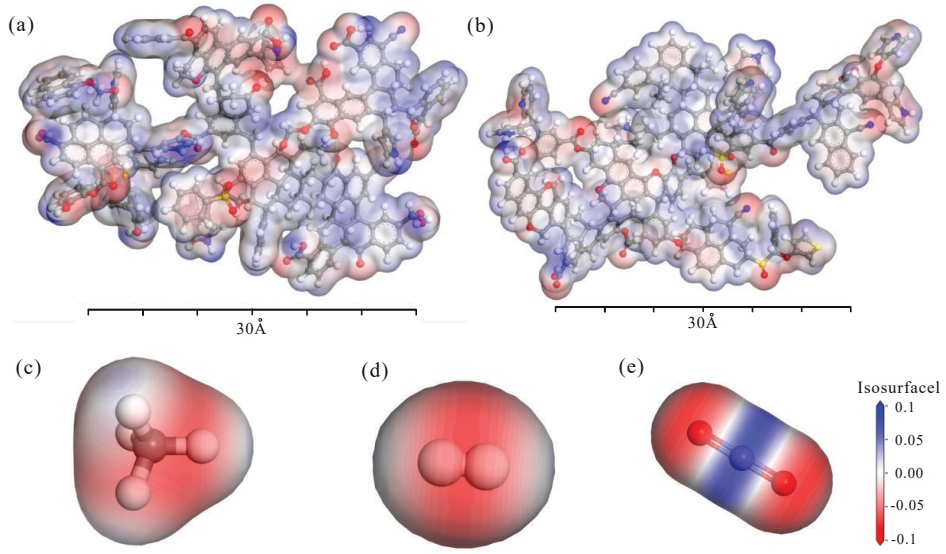



**Fig. 16**. ESP energy spectra of kerogen and gas molecules. (a) GU5 kerogen model, (b) L10 kerogen model, (c) $CH_4$ gas molecule, (d) $H_2$ gas molecule and (e) $CO_2$ gas molecule.

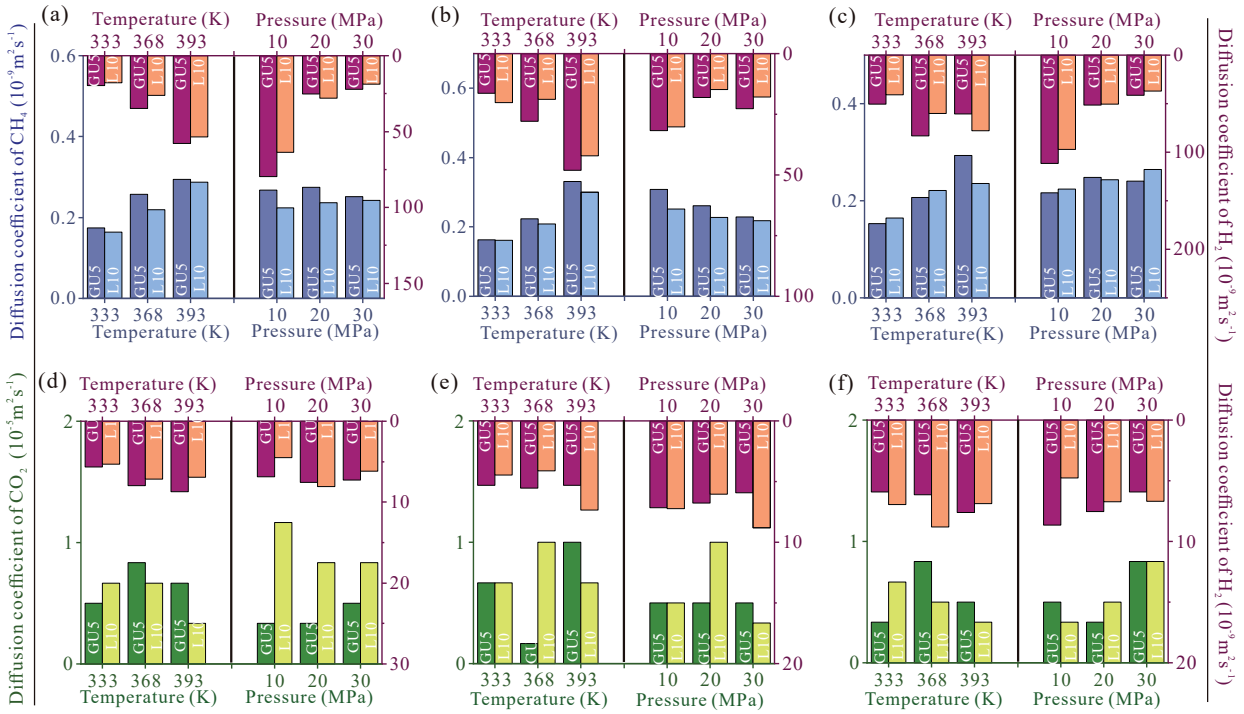



**Fig. 17**. (a)-(c) $CH_4/H_2$ mixtures at ratios of 1:1, 1:3, and 3:1, respectively and (d)-(f) $CO_2/H_2$ mixtures at the same ratios.

security.

## 4.5 Implications for the geological storage of hydrogen under organic-rich shale

Under competitive adsorption conditions, the diffusion coefficients of the mixed gases generally follow the order of $H_2 > CH_4 > CO_2$. Owing to its small molecular size and weak interaction with kerogen, $H_2$ shows the highest mobility and is more easily released into the bulk phase, which may increase its migration tendency and leakage risk during underground hydrogen storage. In contrast, $CO_2$ exhibits the lowest diffusivity because of its stronger affinity for kerogen surfaces and more stable adsorption configuration, while $CH_4$ shows intermediate diffusivity mainly controlled by van der Waals interactions (Chen et al., 2023).

The effect of kerogen maturity is also evident. Compared with high-maturity kerogen, overmature kerogen (Fig. 18) generally exhibits stronger pore confinement and higher near-surface adsorption density (Alanazi et al., 2024), thereby restricting the diffusion of $CH_4$ and $CO_2$ and reducing the effective diffusion space of $H_2$ (Liu et al., 2024b; Zhang et

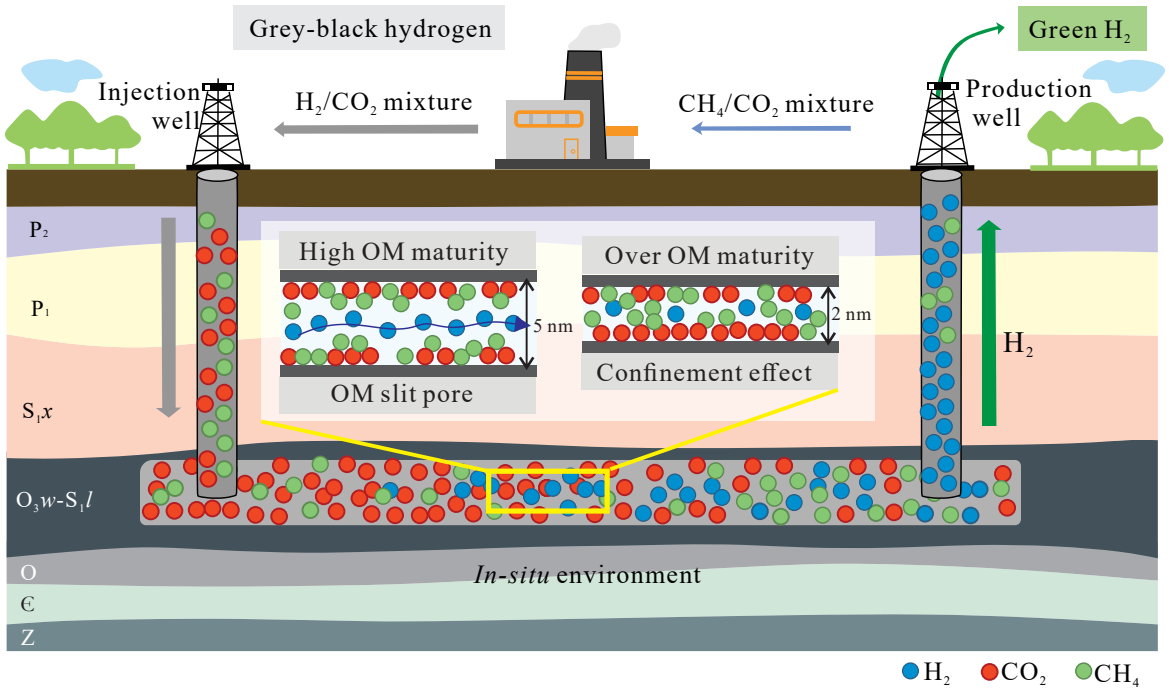



**Fig. 18**. Conceptual model of maturity-controlled competitive adsorption and diffusion of $H_2$, $CH_4$ and $CO_2$ in kerogen nanopores.

al., 2024c). By contrast, the more developed pore network of high-maturity kerogen may facilitate gas transport and enhance the migration tendency of weakly adsorbed $H_2$ (Zhang et al., 2024c). The comparison between $CH_4/H_2$ and $CO_2/H_2$ systems provides important implications for depleted shale reservoirs. In $CH_4/H_2$ systems, residual $CH_4$ preferentially adsorbs on kerogen surfaces and may affect $H_2$ purity, recovery efficiency, and gas mixing during withdrawal. On the other hand, in $CO_2/H_2$ systems, $CO_2$ can act as a cushion gas and occupy high-energy adsorption sites, thereby modifying the available storage and migration space of $H_2$. These results indicate that kerogen maturity and cushion/residual gas composition should be jointly considered when evaluating $H_2$ leakage risk, caprock sealing capacity, and long-term storage performance in organic-rich shale reservoirs.

## 5. Conclusions

This study utilized XPS, FTIR and $^{13}C$ NMR to construct macromolecular models of the Longmaxi kerogen to analyze the competitive adsorption of $CO_2/H_2$ and $CH_4/H_2$. The main conclusions are as follows:

1) The macromolecular structure of Longmaxi kerogen is carbon-dominant, accounting for over 80% of the total elemental composition. The carbon skeleton comprises aromatic, aliphatic and oxygen-containing functional groups. Specifically, the high content of protonated aromatic carbon and branched aromatic carbon indicates that overmature kerogen possesses a more extensive aromatic framework.
2) Kerogen maturity controls the competitive adsorption behavior of $H_2$-bearing gas mixtures by regulating pore confinement and surface properties. Compared with GU5, the more confined pore structure and stronger near-surface interactions in L10 promote the preferential adsorption of $CH_4$ and especially $CO_2$, while limiting the effective adsorption and storage space available for $H_2$.
3) The competitive adsorption mechanisms of $CH_4/H_2$ and $CO_2/H_2$ systems are fundamentally different. $CH_4/H_2$ adsorption is mainly governed by van der Waals interactions, whereas $CO_2/H_2$ adsorption is dominated by stronger electrostatic and inductive interactions. As a result, the adsorption affinity and thermodynamic stability follow the order of $CO_2 > CH_4 > H_2$, and $CO_2$ exhibits the strongest competitive advantage for kerogen adsorption sites.
4) Gas transport in kerogen nanopores is controlled by gas type, competitive adsorption, and maturity-related pore structure, where the diffusion coefficients follow the order of $H_2 > CH_4 > CO_2$. Compared with high-maturity kerogen, overmature kerogen shows stronger pore confinement and higher near-surface adsorption density, which restricts $H_2$ diffusion space and enhances $CH_4/CO_2$ retention. The high mobility of weakly adsorbed $H_2$ indicates a stronger migration tendency and potential leakage risk, highlighting the importance of considering kerogen maturity in evaluating containment security during UHS.

Overall, this study reveals the presence of maturity-controlled coupling between kerogen structure, competitive adsorption and gas transport, providing molecular-scale insights into $H_2$ migration, leakage risk, injectivity, recovery, and storage security in depleted shale reservoirs.

## Acknowledgements

We thank the National Natural Science Foundation of China (Nos. U24A20592, 42472182 and 42272137) for their financial assistance to this research. We also would like to express our sincere gratitude to Khalifa University for providing software support and molecular simulation support.

## Supplementary file

https://doi.org/10.46690/ager.2026.06.07

## Conflicts of interest

The authors declare no competing interest.

**Open Access** This article is distributed under the terms and conditions of the Creative Commons Attribution (CC BY-NC-ND) license, which permits unrestricted use, distribution, and reproduction in any medium, provided the original work is properly cited.

## References

Al-Harbi, A., Abdel-Azeim, S., Saad, M., et al. Adsorption and diffusion behavior of pure $H_2$, and $H_2/CO_2$, $H_2/CH_4$ mixtures in sandstone-rich clay shale reservoirs: Insights from molecular dynamics simulations. International Journal of Hydrogen Energy, 2025, 170: 151214.

Al-Harbi, A., Al-Marri, M., Carchini, G., et al. Hydrogen underground storage in silica-clay shales: Experimental and density functional theory investigation. ACS Omega, 2023, 8(48): 45906-45913.

Alanazi, A., Abid, H., Bawazeer, S. A., et al. Hydrogen and carbon dioxide kinetic adsorption and diffusion behavior into organic-rich shale: Implications of mineralogy and organic content. Energy & Fuels, 2024, 38(23): 23009-23024.

Bian, L., Zhao, Z., Wang, X., et al. Degradation of organic matter by radioactive radiation in black shales: An overlooked modification of organic molecular structures. International Journal of Coal Geology, 2025, 309: 104864.

Chen, F., Mehana, M., Nasrabadi, H. Molecular simulation of hydrogen-shale gas system phase behavior under multiscale conditions: A molecular-level analysis of hydrogen storage in shale gas reservoirs. Energy & Fuels, 2023, 37(3): 2449-2456.

Chen, Y., Zhou, J., Xian, X., et al. Hydrogen and methane adsorption in shale kerogen: Implications for underground hydrogen storage in depleted shale reservoirs. Journal of Energy Storage, 2026, 141: 119512.

Chen, Y., Zou, C., Mastalerz, M., et al. Applications of micro-fourier transform infrared spectroscopy (FTIR) in the geological sciences-a review. International Journal of Molecular Sciences, 2015, 16(12): 30223-30250.

Gomez-Neita, J. S., Mizusaki, A. M. P., da Silva, T. F., et al. FTIR spectral signatures of cretaceous-paleogene subbituminous and bituminous coal: Insights into molecular structure evolution during coalification in the eastern cordillera basin, colombian andes. International Journal of Coal Geology, 2025, 308: 104844.

Gustavsson, L., Haus, S., Lundblad, M., et al. Climate change effects of forestry and substitution of carbon-intensive materials and fossil fuels. Renewable and Sustainable Energy Reviews, 2017, 67: 612-624.

He, J., Ju, Y., Lammers, L., et al. Tortuosity of kerogen pore structure to gas diffusion at molecular- and nano-scales: A molecular dynamics simulation. Chemical Engineering Science, 2020, 215: 115460.

Hou, D., Qiu, X., Gong, F., et al. Characterization of kerogen molecular structure and its effect on methane adsorption behavior: A comparative study on outcrop and core samples from Longmaxi shale. Chemical Engineering Journal, 2023, 466: 143293.

Jiang, Z., Song, Y., Tang, X., et al. Controlling factors of marine shale gas differential enrichment in southern China. Petroleum Exploration and Development, 2020, 47(3): 661-673.

Li, X., Sun, X., Walters, C. C., et al. $H_2$, $CH_4$ and $CO_2$ adsorption on cameo coal: Insights into the role of cushion gas in hydrogen geological storage. International Journal of Hydrogen Energy, 2024, 50: 879-892.

Liang, Z., Jiang, Z., Xue, Z., et al. Molecular structure and evolution mechanism of shale kerogen: Insights from thermal simulation and spectroscopic analysis. Journal of Analytical and Applied Pyrolysis, 2024, 181: 106648.

Liu, J., Zhang, T., Pang, S., et al. Thermal effects of organic porous media on absorption and desorption behaviors of carbon dioxide. Applied Thermal Engineering, 2024, 254: 123920.

Liu, J., Zhang, T., Sun, S. Molecular mechanisms of hydrogen leakage through caprock in moisture and residual gas conditions: A molecular dynamics–Monte Carlo study. Physics of Fluids, 2024, 36(2): 022024.

Liu, Y., Liu, S., Zhang, R., et al. The molecular model of Marcellus shale kerogen: Experimental characterization and structure reconstruction. International Journal of Coal Geology, 2021, 246: 103833.

Mohammed, I., Al-Yaseri, A., Bello, A., et al. Shale electrokinetic property and colloidal stability: Potential for subsurface $CO_2$ storage. Energy & Fuels, 2023, 38(2): 1111-1125.

Mohr, S. H., Wang, J., Ellem, G., et al. Projection of world fossil fuels by country. Fuel, 2015, 141: 120-135.

Navaid, H. B., Emadi, H., Watson, M. A comprehensive literature review on the challenges associated with underground hydrogen storage. International Journal of Hydrogen Energy, 2023, 48(28): 10603-10635.

Oye, O. J. Integrated reflection-ftir and multivariate partial least squares approach for rapid and accurate assessment of total organic carbon concentration in shale. Journal of Petroleum Science and Engineering, 2022, 217: 110912.

Pan, S., Zhou, H., Wang, Q., et al. Experimental and molecular simulation studies of Huadian oil shale kerogen. ACS Omega, 2022, 7(20): 17253-17269.

Psarras, P., Holmes, R., Vishal, V., et al. Methane and $CO_2$ adsorption capacities of kerogen in the Eagle Ford shale from molecular simulation. Accounts of Chemical Research, 2017, 50(8): 1818-1828.

Raza, A., Alafnan, S., Glatz, G., et al. Geo-storage of hydrogen in organic-rich shales: Multicomponent selectivity of

organic nanopores. Fuel, 2024, 359: 130476.

Ren, J., Sun, L., Li, X., et al. Interfacial dynamics and mass transfer in underground hydrogen storage applications: A review of $H_2$ flow, stability and storage performance. Advances in Geo-Energy Research, 2025, 18(2): 121-136.

Sekar, L. K., Kiran, R., Okoroafor, E. R., et al. Review of reservoir challenges associated with subsurface hydrogen storage and recovery in depleted oil and gas reservoirs. Journal of Energy Storage, 2023, 72: 108605.

Sikiru, S., Soleimani, H., Rostami, A., et al. Analysis of $CH_4$ and $H_2$ adsorption on heterogeneous shale surfaces using a molecular dynamics approach. Fluid Dynamics & Materials Processing, 2024, 20(1): 31-44.

Sun, H., Ren, P., Fried, J. R. The compass force field: Parameterization and validation for phosphazenes. Computational and Theoretical Polymer Science, 1998, 8(1-2): 229-246.

Sun, Z., Shi, J., Wu, K., et al. Gas flow behavior through inorganic nanopores in shale considering confinement effect and moisture content. Industrial & Engineering Chemistry Research, 2018, 57(9): 3430-3440.

Suzuki, N., Saito, H., Hoshino, T. Hydrogen gas of organic origin in shales and metapelites. International Journal of Coal Geology, 2017, 173: 227-236.

Tarkowski, R., Uliasz-Misiak, B. Towards underground hydrogen storage: A review of barriers. Renewable and Sustainable Energy Reviews, 2022, 162: 112451.

Tian, S., Wang, T., Li, G., et al. Nanoscale surface properties of organic matter and clay minerals in shale. Langmuir, 2019, 35(17): 5711-5718.

Waldman, M., Hagler, A. T. New combining rules for rare gas van der Waals parameters. Journal of Computational Chemistry, 2004, 14(9): 1077-1084.

Wang, C., Zhao, Y., Wu, R., et al. Shale reservoir storage of hydrogen: Adsorption and diffusion on shale. Fuel, 2024, 357: 129919.

Wang, Y., Wei, G., Shen, J., et al. Analysis on distribution and main controlling factors of OM carbonization in marine shale in the Sichuan Basin of China and its periphery. Journal of Natural Gas Geoscience, 2022, 7(4): 181-197.

Wu, W., Cheng, P., Luo, C., et al. Gas-in-place content of deep shales and its main controlling factors: A case study on the Wufeng-Longmaxi shales in the middle Luzhou block of the southern Sichuan Basin, China. Energy & Fuels, 2023, 37(12): 8296-8310.

Xiong, F., Wang, A., Chen, J., et al. Densities and other thermodynamic parameters of supercritical hydrogen adsorption on coals. Chemical Engineering Journal, 2026, 528: 172539.

Yang, Y., Neil, C. W., Guiltinan, E. J., et al. Experimental characterization of hydrogen diffusion in shale rocks for geologic storage applications. ACS Earth and Space Chemistry, 2025, 9(7): 1858-1870.

Yu, M., Wang, K., Vredenburg, H. Insights into low-carbon hydrogen production methods: Green, blue and aqua hydrogen. International Journal of Hydrogen Energy, 2021, 46(41): 21261-21273.

Zhang, H., Diao, R., Luo, X., et al. Molecular simulation of $H_2/CH_4$ mixture storage and adsorption in kaolinite nanopores for underground hydrogen storage. ACS Omega, 2023, 8(48): 45801-45816.

Zhang, M., Yang, Y., Pan, B., et al. Molecular simulation on $H_2$ adsorption in nanopores and effects of cushion gas: Implications for underground hydrogen storage in shale reservoirs. Fuel, 2024, 361: 130621.

Zhang, Q., Masoudi, M., Sun, L., et al. Hydrogen and cushion gas adsorption-desorption dynamics on clay minerals. ACS Applied Materials & Interfaces, 2024, 16(40): 53994-54006.

Zhang, T., Liu, J., Yang, X., et al. Advances in the microscopic and mesoscopic simulation technologies developed for subsurface gas storage. Advances in Geo-Energy Research, 2024, 14(1): 1-3.

Zhao, Y., Quan, D., Wang, C., et al. Experiments and molecular simulations study on hydrogen adsorption and diffusion behavior of the inorganic mineral surfaces of shale. International Journal of Hydrogen Energy, 2025, 97: 1302-1315.

Zou, C., Zhu, R., Chen, Z., et al. Organic-matter-rich shales of China. Earth-Science Reviews, 2019, 189: 51-78.